Preparation of Blackened Ca-based Composite Particles and Their Carbonation Kinetics Features

Liang Teng[1], Yimin Xuan[*,1], Xianglei Liu[1],and Yulong Ding[2]
[1] College of Energy and Power Engineering, Nanjing University of Aeronautics and Astronautics, Nanjing 210016, China
[2] Birmingham Centre for Energy Storage (BCES), School of Chemical Engineering, University of Birmingham, Birmingham B15 2TT, UK
*Corresponding author E-mail address: ymxuan@nuaa.edu.cn

Abstract

The calcium looping (CaL) thermochemical thermal energy storage is one of the best high-temperature heat storage schemes for 3th concentrating solar power (CSP) photothermal power. Before this technology being widely employed, however, the inherent low solar absorption capability and poor cyclic stability of $CaCO_3$/CaO based material need to be overcome. In the present work, the solar absorbing capability of $CaCO_3$ particles is enhanced by doping Mn-Fe oxides, meanwhile, awns of setaria faberis (ASF) and microcrystalline cellulose (MCC) are used as bio-templates to generate pores inside the particles. The pore-making process promotes the cyclic stability and carbonation kinetic features of the composite particles simultaneously. The test results show that the proposed particles possess adequate anti-crushing strength, high cyclic stability, high solar absorption, and high carbonation rate. In addition, the carbonation kinetic features of the composite porous particles are studied with the influence factors such as CO_2 partial pressure, reaction temperature, and particle morphology taken into consideration. A kinetic equation involving these parameters is developed with the thermogravimetry data of the prepared samples. By employing this kinetice function, the carbonation reaction of the prepared particles inside the carbonator becomes predictable, which is of great significance for the design and regulation of the carbonator achieving highly stable heat output in the CaL thermochemical heat storage system.

Keywords: Calcium looping (CaL); Thermochemical heat storage; Porous particles;

Kinetics features

1 Introduction

Clean and renewable new energy sources are playing an increasingly important role in human energy systems. As one of the most promising new energy utilization technologies, concentrating solar power (CSP) generation technology has been included in the energy development plans of many countries [1, 2]. High-temperature thermal energy storage (TES) becomes one of the key technologies for CSP system because it plays an important role in overcoming the inherent intermittency and instability of solar energy [3-5]. The target operating temperature of the next generation of CSP technology exceeds 700 °C, which brings more challenges to the TES system [2, 6, 7]. Sensible heat storage materials commonly possess low heat storage densities, thus they commonly require large hot tank capacity and higher storage temperature, which cause a great amount of heat loss. Most latent heat storage materials for high-temperature operating are expensive and they might cause serious corrosion of the storage tank. The thermochemical heat storage technology based on the decomposition reaction of $CaCO_3$ and carbonation reaction of CaO becomes one of the most promising TES schemes for 3th CSP systems [8-13]. The working principle of the integrated CaL-CSP system is indicated in Fig. 1 [14, 15]. The revisable reaction is described by the chemical formula [16]:

$$CaCO_3(s) \rightleftharpoons CaO(s)+CO_2(g) \quad \Delta H_{298\,K}=+178\ kJ/mol \tag{1}$$

The $CaCO_3$ material comes from a wide range of sources and it is safe and non-toxic, moreover, the reaction temperature is appropriate for the operating temperature over 700 °C[11-13, 17, 18].

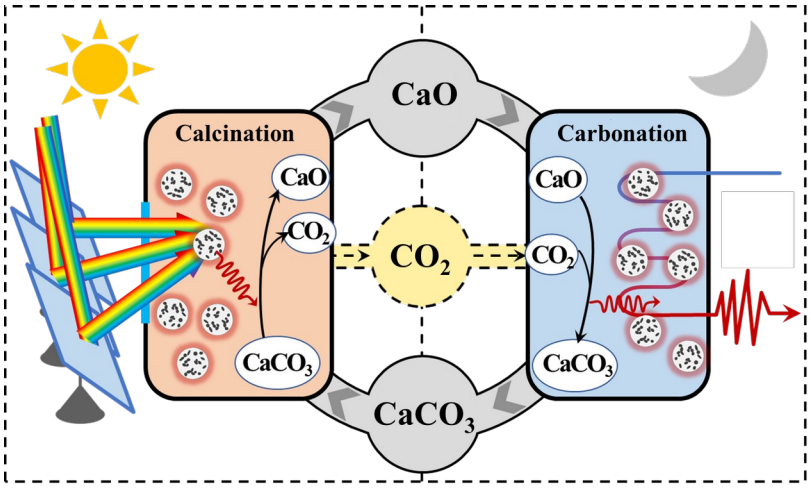

Fig. 1. Schematic diagram of the solar driven CaL thermochemical TES system.

With respect to the calcium looping (CaL) based TES technologies being applied in CSP systems, however, two inherent defects related to calcium-based materials need to be addressed [19-23]. The $CaCO_3$ material has low absorption capability for directly capturing solar energy, thus most current solar-driven $CaCO_3$ calcinators employ the solar absorptive coating to absorb solar heat and then transfer the heat to the internal $CaCO_3$ by means of heat conduction through the wall [24-29]. This indirect heating mode brings about additional thermal resistance and heat loss during the calcination process. Another drawback of $CaCO_3$ is that it is easy to get sintered at the operating temperature [30-33]. The Tammanm temperature of $CaCO_3$ is ~533 °C while the operating temperature ranges from 650 °C to 850 °C, as a result, the $CaCO_3$ granules are severely agglomerated and the chemical reactivity of the sintered body dramatically declines. Along with the increasing cycle number, the conversion rate of CaO particles decreases rapidly, as well as the heat release amount and rate. Moreover, for the convenience of transport and storage, $CaCO_3$/CaO is commonly made into solid particles in the practical application. The commonly used CaO particles possess low porosities, and the pores gradually close up during the carbonation process hence the reaction proceeds slowly from the outer layer to the center of the particle via the diffusion of molecules and ions. This low reaction rate results in a low heat release power of the thermochemical heat storage system. The

poor cyclic performance and low exothermic (carbonation) reaction rate have become great challenges to the CaL thermochemical heat storage technology. To solve these problems, the approach to prepare porous $CaCO_3$ particles with excellent gas permeability and large specific surface area is needed.

In addition to the design and preparation of composite porous particles, the investigation of their kinetic features also deserves more attention. The heat output power from the thermochemical heat storage system is largely dependent on the exothermic reaction rate [34, 35]. Accordingly, the carbonation kinetic features of the composite porous particles are one of the most essential elements and considerations for the design and regulation of carbonator. The carbonation reaction rate is affected by many factors such as reaction temperature, CO_2 partial pressure, and particle morphology. The lack of precise information about the carbonation process of the prepared composite porous particle under these operating conditions will directly cause the failure of carbonator design. Therefore, it is necessary to establish a carbonation kinetic model containing relevant parameters to describe the chemical reaction of the prepared particles inside the carbonator.

In our previous work, the dopant materials Mn-Fe oxides were used to adjust the spectral feature of $CaCO_3$, and the modified composite material directly and efficiently absorbed solar radiation [17]. However, the powdery materials are not suitable for the large-scale industrial applications and they are easily inhaled into the body and pose serious harms to human health. Therefore, in this work, we will further improve the preparation process in order to develop a Ca-based composite particle capable of directly and efficiently absorbing solar radiation. Furthermore, for the sake of highly stable heat storage cycles and excellent carbonation kinetic features, the template synthesis method is used to generate porous-structure inside the particles. Herein, for the first time, the awns of Setaria faberi (ASF) are used as templates to create macro strip holes inside the particles, which is expected to perforate the particle and reduce the number of blind holes. The CO_2 gas is capable to permeate into the

particles and react with CaO on the inner interface and outer surface at the same time. The carbonation process of the prepared particles is analyzed under the isothermal conditions. A kinetic model containing the partial pressure of CO_2 and the morphology parameters of composite porous calcium-based particles is established based on the conventional kinetic equation. The proposed kinetic model is expected to be of positive significance to the prediction of the carbonation process of calcium-based composite particles and the optimization of the particle preparation process.

2 Experimental Section

2.2 Materials

All the chemical reagents used in the experiment are of analytically pure grade, and they are used directly without further purification. The ferric nitrate nonahydrate ($Fe(NO_3)_3 \cdot 9H_2O$), manganese nitrate solution (50%, $Mn(NO_3)_2$), calcium hydroxide ($Ca(OH)_2$) powder, and aluminum oxide Al_2O_3 (γ) powder are purchased from Shanghai Aladdin Biotechnology Co., Ltd, China.

Two kinds of materials are used as the pore-making templates. The first one is the awns of setaria faberis (ASF) and the other one is the microcrystalline cellulose (MCC, Tianjin Berens Biotechnology Co., Ltd). The panicles of setaria faberis are collected in summer from the campus located in Nanjing, China. These panicles are firstly dried in the electric oven at 200°C for 6 hours and are then pounded with mortar and pestle to separate the awn from the seeds. At last, the awns are screened out by a steel-wire screen with the mesh size of 100 μm.

2.3 Preparation processes

The preparation process of particles is exhibited in Fig. 2. The mixed solution of $Fe(NO_3)_3$ and $Mn(NO_3)_2$ (mole ratio of 2:1) is slowly dropped into $Ca(OH)_2$ and Al_2O_3 mixed powder, and the wet mixture materials are constantly stirred until it is fully homogeneous. Then the pore-making template is added to the mixture, which is also followed by stirring until well mixed. Next, the mixture is added to the screw extruder, by which materials can be made into strips with the diameter of 0.8 mm.

These trips are divided into cylinders with a length of about 0.8mm and cylindrical particles are rounded into spherical particles in the rounding machine. After that these spherical particles are calcined in the muffle furnace at 700 °C for 3h and at last, they are carbonated in a tube furnace with flowing pure CO_2 at the 700 °C for 3h. By following the above operating procedures, the solid particles with different composition ratios are fabricated. The particle samples are termed as M_{Ca}-M_{Al}-M_{Mn}-M_{Fe}-m_{MCC}-m_{ASF}, where M is the molar proportion and m is the mass of used template material per 10 g $CaCO_3$. In our previous work, a kind of $CaCO_3$/Mn-Fe-O composite material was developed and the proposed material shows excellent solar absorbing capability[17]. The molar ratio of Ca:Mn:Fe in that composite material is 100:6:12, and this proportion will also be used in this work. Additionally, Al_2O_3 is doped into the particles to enhance the strength of the particles. According to a number of primary experimental tests, and the molar ratio Ca:Al=100:15 is selected in this work.

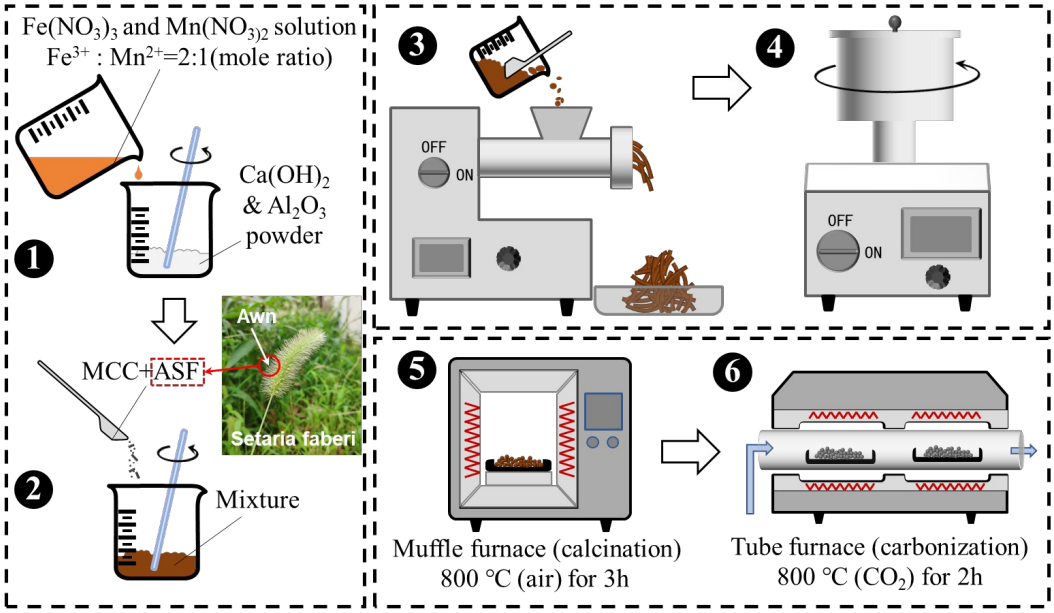

Fig. 2. Preparation procedures of porous composite particles

2.4 Cycling stability measurements

The cyclic performances of the fabricated particles are measured with a thermogravimetric (TG) analysis device (STD 650, TA Instrument). The inert gas of the calcinator greatly impacts the reaction temperature and system operating costs. A

great number of researches on CaL thermochemical heat storage employ CO_2 as the inert gas because the CO_2 can be reused as the particle carrier-gas without any gas separation equipment. However, the increment of CO_2 partial pressure leads to the rise in the calcination temperature and then results in the intensification of sintering and a shorter service life of the heat storage material. Here two calcination conditions are considered: the pure Ar used to simulate the calcination under low CO_2 concentration and the pure CO_2 relating to the application with high CO_2 partial pressure and reaction temperature. In the first case, the reaction temperatures for both calcination and carbonation are 750 °C, and the surrounding atmospheres are pure Ar and pure CO_2, and reaction times are 15 min and 20 min, respectively. For another cyclic condition, both calcination and carbonation processes proceed in pure CO_2. The operating temperature and reaction time for calcination are 900 °C and 10 min and those for carbonation are 750 °C and 20 min, respectively.

2.5 Kinetic measurement

Within a high-temperature (over 700 °C) thermochemical heat storage system, a stable heat-releasing temperature is required to supply a steady heat source for the thermodynamic unit. Therefore, the isothermal exothermal characters of the heat storage material and relevant regulation method is essential for the CaL based thermochemical heat storage technology. Many factors affect the exothermic reaction of particles, including particle morphology, reaction time, temperature, pressure, etc. In order to reveal the influence of these factors on the carbonation of the proposed particle, the carbonation kinetics is studied utilizing the thermogravimetric analysis (TGA). This work focuses on the carbonation process of the synthetic particle within the temperature range from 700 °C to 800 °C.

Different from previous researches on the non-isothermal carbonation of CaO for the application of carbon capture, the present study focuses on the isothermal carbonation at over 700 °C for the utilization of the thermochemical TES system [36, 37]. The isothermal method is used to analyze the carbonation process of composite

particles. Because a stable carbonation temperature is needed to achieve steady heat release in the Cal thermochemical heat storage system. In the isothermal experiment, the particles are carbonated in a thermogravimetric analysis device (STD 650, TA Instrument) at the constant temperatures of 700 °C, 725 °C, 750 °C, 775 °C, and 800 °C. The CaO composite particles used in carbonate kinetic measurements come from the sample 100-15-6-12-1.5-0.5 after the first calcination at 800 °C.

2.6 Samples characterization

The micro-morphologies and microstructures of the samples are observed with a scanning electron microscope (SEM) devices (Gemini 300, ZEISS) and computerized tomography (CT) scanner (Phoenix Nanotom S, General Electric Company). The awns of setaria faberis are observed with a confocal microscope devise from OLYMPUS (LEXT OLS5000).

The anti-crushing strength is measured by recording the peak pressure at the crushing moment of particles using a precision pressure testing equipment from JiNan LinYue accurate instrument Co,. Ltd (LYYS-100N). During the measurement, ten particles are randomly chosen as test subjects from each particle sample.

The crystalline phase compositions of the synthetic materials were measured by an X-ray diffraction equipment (D8 ADVANCE, Bruker). Before the measurement is conducted, the sample particles are grounded into powders with a mortar.

The spectral reflectance of the particle samples is measured with an ultraviolet and visible (UV/VIS) spectrophotometer (Lambda 1050, PERKINELMER). The particles are enclosed in a circular sample cell (Φ15mm×3mm) covered by a quartz plate. The transmittance is considered to be zero, and absorptance is calculated by subtracting reflectance from 100%. It should be noted that the quartz plate is not an ideal transparent body, thus the measure spectral absorption is lower than the real value.

The specific surface areas are measured by a physical adsorption meter (ASAP 2460, Micromeritics) using Brunauer–Emmett–Teller (BET) theory. The particles are

screened by stainless steel wire sieve with the mesh size of 0.6 mm and 1 mm. The mean diameter is calculated by dividing the total length of a row of tightly arranged particles with the total number. The mean mass of the particle is measure by a precision balance.

3 Results and discussion

3.1 Particle morphology

The photomicrograph of the ASF is shown in Fig. 3a. The surface grain of ASF is similar to that on the inner wall of the strip holes shown in Fig. 3d and Fig. 3e. The comparison photograph of particles and ruler is presented in Fig. 3b, the mean diameter of the prepared particles is ~0.8mm. The CT image shows that strip holes irregularly distribute inside the particles. These channels are dozens of microns in diameter, which are expected to promote the gas transport capacity of the particle and reduce the characteristic diameter of the particle. Except for the strip holes, there are also some irregular micro-holes inside the particles, which are marked by red circles in Fig. 3d and 3e. A minority of these micro-holes joint with the trip holes and most of them are blind holes. The cross-section SEM (Fig. 3e) illustrates that the ashes of the calcinated ASF stay inside the particles since the calcination treatment. Similarly, MCC ashes also remain in the pores and become part of the synthetic particles. The effect of these ashes on gas transport is negligible because they are porous and their profiles are smaller than that of holes, while on the other hand the ASF ashes remarkably impact the solar absorption capacity of particles. The influences of ashes on the optical properties of fabricated particles are detailly discussed in section 3.3.

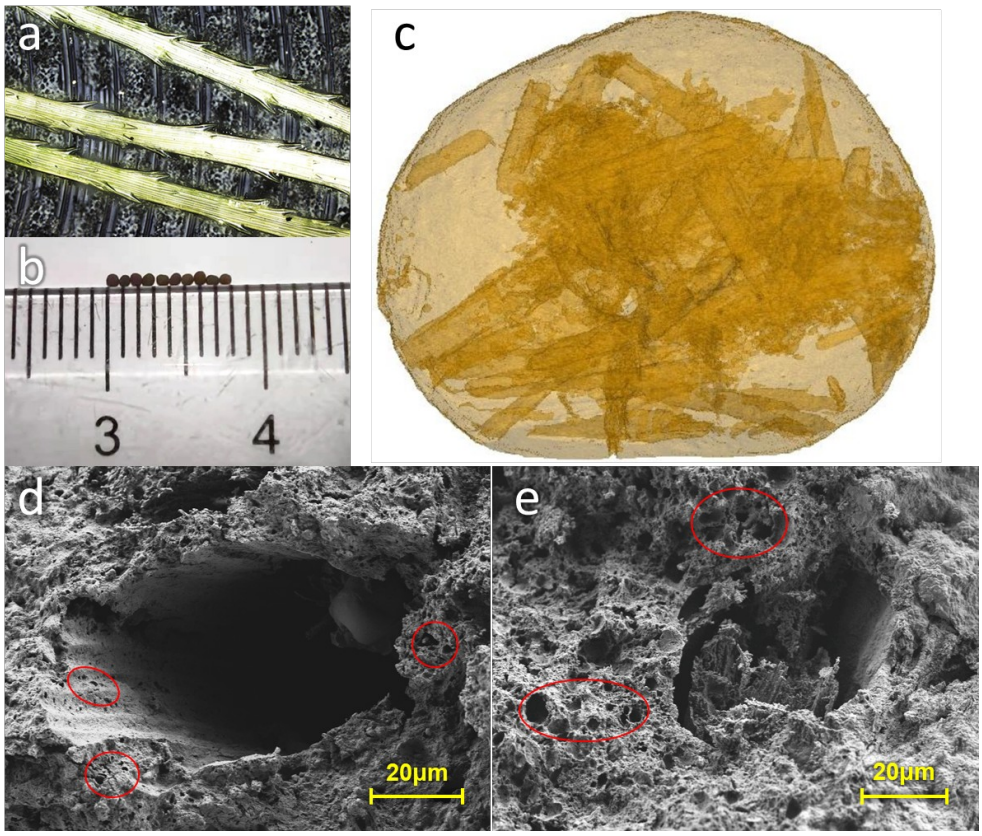

Fig. 3 a: photomicrographs of the ASF; d: photograph of the fabricated particles; c: CT image of a particle using ASF as pore making template; d, e: SEM images of pores on the particle cross-section

3.2 Mechanical strength and cyclic performance

The anti-crushing strength results are numbered and shown in Fig. 4. The short horizontal lines in the figure represent the arithmetic mean values. The red dotted line indicates the demand for the anti-crushing strength of particles in a continuous operating fluidized bed [38, 39].

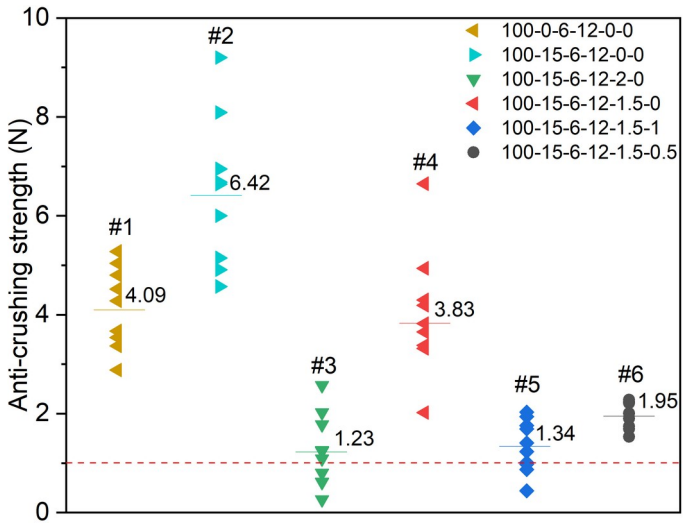

Fig. 4 Anti-crushing strength of different particles

Sample #2 (as numbered in Fig. 4) has higher average anti-crushing strength than sample #1, which illustrates that the mechanical strength of particles is enhanced by the Al element existing in the composite material. The anti-crushing strength of the composite material remarkably decreases after the pore-forming procedure, as demonstrated by the strength difference between sample #2 and sample #3, #4, #5, #6. The higher usage amount of templates relates to the larger porosity of the particle and higher reactivity but at the same time lower anti-crushing strength. Generally, the solid particles with the anti-crushing strength above 1 N (marked by the red dotted line in Fig. 4) show adequate durability in continuously operating fluidized bed [38, 39]. The test results show that part of the particles in samples #3 and #5 possess anti-crushing strength lower than 1, which implies that the template usage amount of these two samples should be decreased. With fewer templates used, sample #4 and #5 show obvious promotion on the mechanical property. Compared to #3 and #5, the average anti-crushing strengths of sample #4 and #6 increase for 2.60 N and 0.61 N respectively, and none of the test particles in #4 and #6 has anti-crushing strength below 1 N. Therefore, the composite porous particle numbered by #4 and #6 is deemed to be available for the application in fluidized bed reactor.

The cyclic experiments of three samples under two different conditions are conducted and the results are illustrated in Fig. 5, in which 750Ar/750CO_2 and

$900CO_2/750CO_2$ represent that the calcination temperature and atmosphere are repectively maintained at 750 °C and 900 °C under pure Ar or CO_2. Similarly, both their reaction conditions for carbonation are 750 °C and pure CO_2.

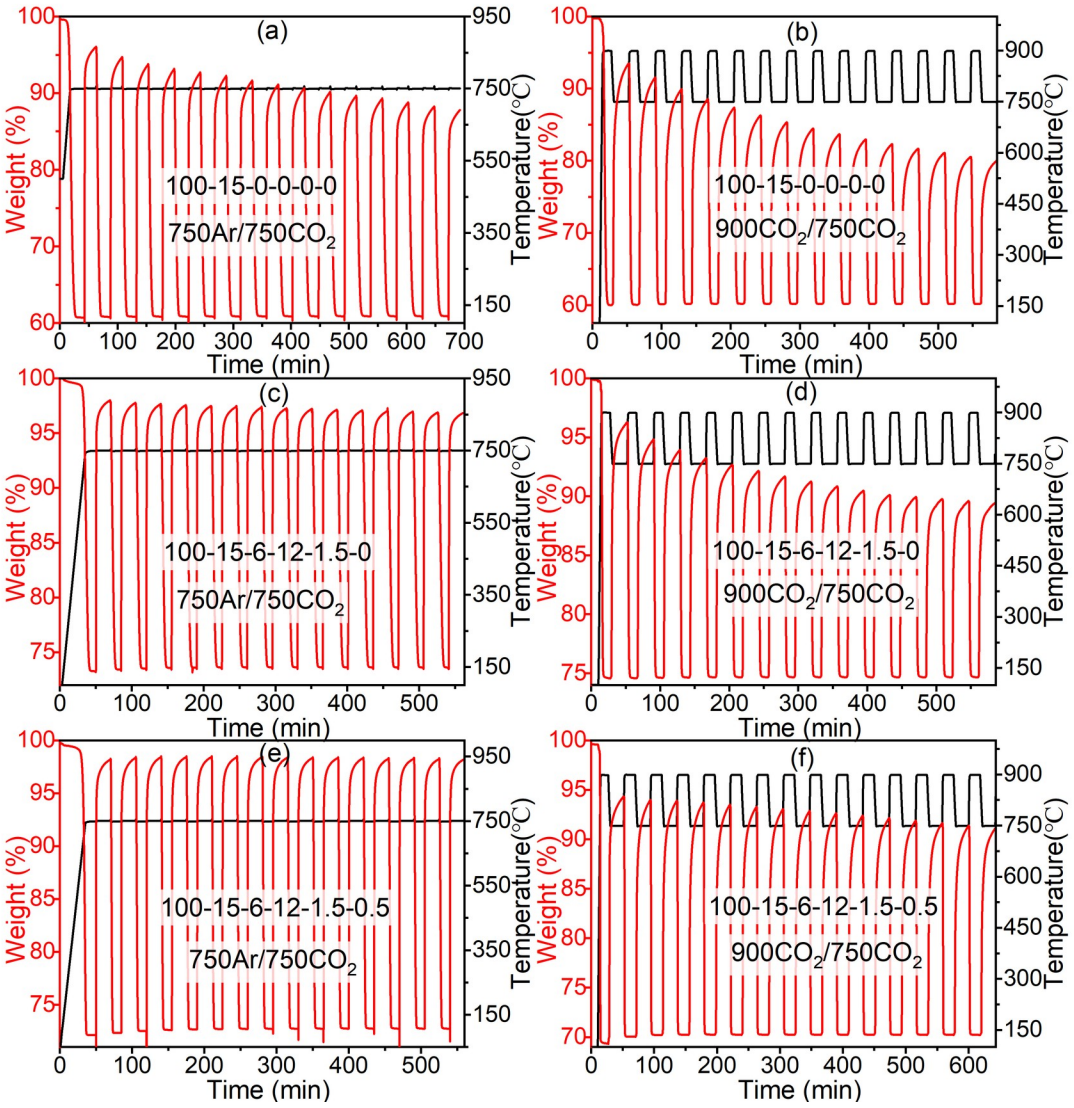

Fig. 5 Thermogravimetric diagrams of cyclic experiment: a, c, e and b, d, f show the results tested with pure Ar and CO_2 as calcination atmosphere, respectively

Using the TG data exhibited in Fig. 6 a-f, the heat release efficiencies of the particles are computed through the followed expression:

$$\eta_{r,N} = \frac{m_{car,N} - m_{cal,N}}{m_1 - m_{cal,N}} \tag{2}$$

where $m_{car,N}$ and $m_{cal,N}$ represent for the mass of the sample after the carbonation and

calcination in cycle *N* respectively, m_1 refers to the initial mass of the sample before the cycles. Heat release efficiency is the ratio of released heat in each cycle to the total stored heat of the particles [17]. This parameter indicates the heat releasing capability of calcium-based particles during the heat storage cycles. As shown in Fig. 6, the sample 100-15-0-0-0-0 shows lower heat release efficiencies and continuous attenuation in followed cycles under both cyclic conditions compared to the porous particles doped with Mn-Fe oxides. Once the calcination temperature increases from 750 °C to 900 °C, the thermochemical heat storage efficiencies of all these three samples decay faster along with the increasing cycle number, but the porous particles containing Mn-Fe oxides still behave lower attenuation rates than other Ca-Al particles do. With additional ASF used as pore-forming templates, the sample 100-15-6-12-1.5-0.5 shows higher and more stable heat storage efficiencies than sample 100-15-6-12-1.5-0. Meanwhile, its anti-crushing strength satisfies the mechanical strength requirement. Therefore, sample 100-15-6-12-1.5-0.5 is more suitable for the application in CaL based thermochemical heat storage system.

On the one hand, the dopant materials (Mn-Fe oxides) modify the optical properties of $CaCO_3$, but on the other hand these inactive ingredients also lead to the decrement of the thermochemical heat storage density of the composite material. The thermochemical heat storage density D_N is expressed as:

$$D_N = \frac{\left(m_{car,N} - m_{cal,N}\right) \Delta H / M_{CO_2}}{m_1} \tag{3}$$

where ΔH is the reaction enthalpy of Eq. (1), M_{CO2} is the molar mass of CO_2. The calculated thermochemical heat storage densities are presented in Fig. 6b. It is illustrated that the Ca-Al particles possess larger thermochemical heat storage densities than the particles doped with Mn-Fe oxides within the first 15 cycles. But it is obvious that the thermochemical heat storage density of the Ca-Al rapidly decreases as the cycle number increasing. The decline proportion in 15 cycles is 35 % and 0 for

sample 100-15-0-0-0-0 and sample 100-15-6-12-1.5-0.5, respectively. According to the tendencies, therefore, the sample 100-15-6-12-1.5-0.5 shows higher stability and is expected to possess larger thermochemical heat storage densities in the whole life period. Besides, by comparing the results obtained under different operating temperatures, one can find that the superiority of porous Ca-Al-Mn-Fe particles on withstanding the sintering becomes more obvious under higher operating temperatures compared to the Ca-Al particles. The thermochemical heat storage density of the former exceeds that of the latter one in the dozenth cycle.

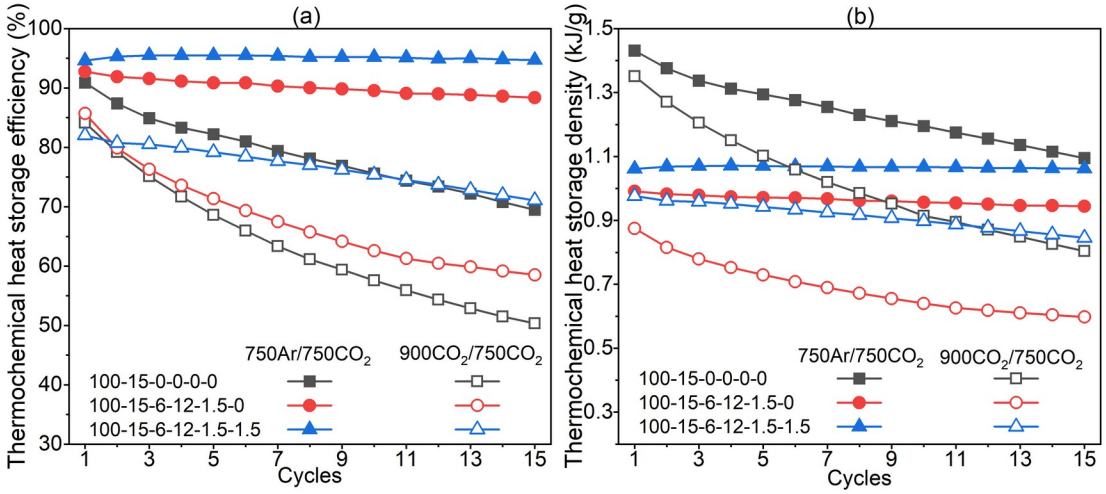

Fig. 6. a: thermochemical heat storage efficiency and b: thermochemical heat storage density diagrams

3.3 Phase composition and optical propertie

The XRD patterns of the synthetic particles are presented in Fig. 7. It is indicated in the figure that most of the diffraction peaks of the Ca-Al particle (sample 100-15-0-0-0-0) belong to the $CaCO_3$ owing to the high content of Ca element and high crystallinity of $CaCO_3$. The diffraction peak of aluminiferous oxide is not found in the patterns, of which the possible cause might be the low crystallinity and the high recrystallization temperature (1200 °C, above the preparation temperature) of the used γ Al_2O_3 powder. After introducing the Mn-Fe oxides, several kinds of nonstoichiometric polymetallic oxides containing Mn and Fe are founded in the synthetic particles. These polymetallic oxides play a key role in enhancing the solar spectral absorption capability of the composite material. It is attributed to the high

photons-absorbing features of the electron orbital of Mn^{2+} and Fe^{3+} in the solar spectrum [17]. The spectral absorption of the pure Mn-Fe-oxide tablet is shown in Fig. 8, which verifies the high solar absorption capability of the Mn-Fe oxides. The SEM image (Fig. 3e) shows that the ASF ashes (K_2O, P_2O_5, etc) stay inside the particle pores, but there is no impurity peak corresponding with ASF component in the XRD patterns, which mainly results from the low usage amount of ASF.

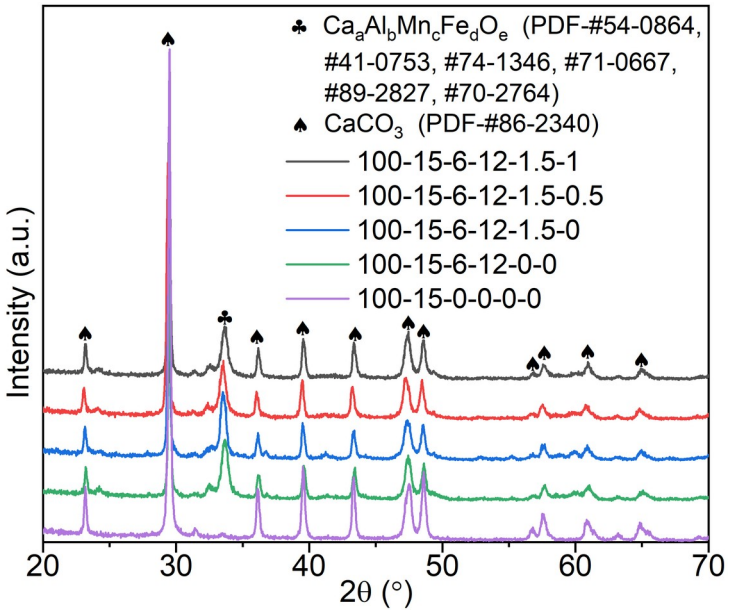

Fig. 7 X-ray diffraction (XRD) analysis results of particle samples

The solar spectral absorptance of the calcium-based composite particles containing Mn and Fe are exhibited in Fig. 8a. Using these spectral absorptances and AM1.5D data, the average solar absorption of the synthetic particles can be computed and the math expression is given by:

$$A_{sol} = \frac{\int_{300nm}^{2500nm} \alpha(\lambda) I_{AM1.5D}(\lambda) d\lambda}{\int_{300nm}^{2500nm} I(\lambda)_{AM1.5D} d\lambda} \tag{4}$$

where $\alpha(\lambda)$, $I_{AM1.5D}(\lambda)$ respect the measured spectral absorptance and spectral irradiance under AM1.5D conditions, respectively, λ stands for the wavelength. As presented in Fig. 8b. the average solar absorptance of Ca-Al particles is 23.00%,

while those of the porous Ca-Al-Mn-Fe particles are 88.14%, 85.25%, and 78.98%, respectively.

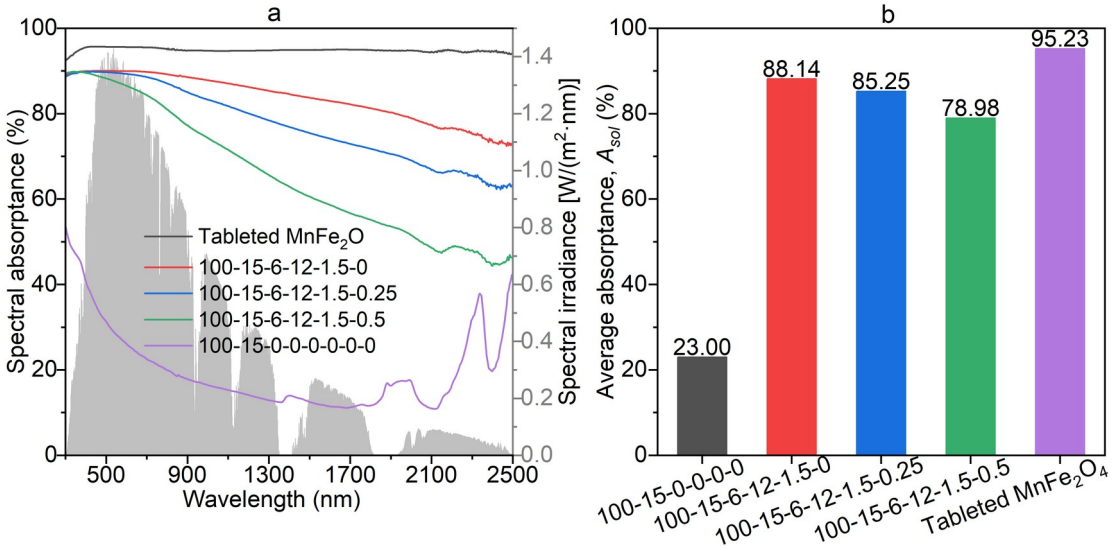

Fig. 8 a: spectral absorptances and b: average solar absorptances of particle samples

Moreover, it is indicated that the spectral absorptance and average solar absorptance decrease along with the increment of the amount of used ASF template. That is because the ash (metallic oxide) left in the pore of particles possess a low solar absorptance, therefore a larger usage amount of the ASF leads to a lower solar absorptance.

The prepared composite particles exhibit benign solar absorbing capability, cyclic stability, and crushing resistance. Different amounts of the used pore-making materials obtain different performance advantages. The sample 100-15-6-12-1.5-0 is superior in terms of absorbing solar energy, while sample 100-15-6-12-1.5-0.5 has higher stability in the continuous cycle. The test results show that the developed approach is capable to fabricate composite porous particles with a favorable performance for the application of a solar-driven CaL thermochemical heat storage system.

4 The thermal analysis kinetics

The carbonation kinetic features of the particles are important considerations for the design and regulation of the carbonator, therefore a kinetic function calculating the

reaction rate under different conditions are necessary for the application of CaL thermochemical heat storage. The carbonation reaction rate is related to morphological parameters of particles and carbonation conditions, therefore the reaction rate dα/dt is considered to be a function of the specific surface area (A_s), particle average mass(M), particle average diameter (D), the CO_2 partial pressure (P_{CO2}), and reaction temperature (T), as well as the kinetic triplets: dα/dt=F(A_s, M, D, P_{CO2}, T, A, E, $f(\alpha)$). The kinetic function in this work is developed by introducing these parameters into the conventional gas-solid reaction kinetic model in a dimensionless form[34, 40]. The formula is written as:

$$\frac{d\alpha}{dt} = A\frac{A_s M}{D^2}\exp\left(-\frac{E}{RT}\right)\left(\frac{P_{CO_2}-P_{equ}}{P_{atm}}\right)^{m} f(\alpha) \tag{5}$$

$$P_{equ} = 4.137\times10^{12}\exp(-\frac{20474}{T}) \tag{6}$$

where A, E, $f(\alpha)$ are the pre-exponential factor, activation energy, and mechanism function, respectively, P_{CO2}-P_{equ} is the difference between the equilibrium and partial pressure of CO_2, P_{atm} is the atmospheric pressure, m is the reaction order, α is the conversion during carbonation and it can be calculated by:

$$\alpha = \frac{m_{rea}-m_{cal}}{m_{ini}-m_{cal}} \tag{7}$$

where m_{ini} refers to the initial mass of particles, m_{rea} is the real-time mass of particle during carbonation, m_{cal} is the mass after the calcination procedure. The morphological parameters of porous composite CaO particles (sample 100-15-6-12-1.5-0.5 after the first calcination procedure) are presented in Table 1.

Table 1. The main morphological parameters of CaO particles

Parameter	Value	Unit
Mean mass, M	0.273	mg
Mean diameter, D	0.8	mm

Specific surface area, A_s	9.8442	m^2/g

The non-isothermal TGA method using multiple heating rates are not used in this work because the reaction conditions in the non-isothermal measurements remarkably differ from the actual conditions inside the carbonator. In the non-isothermal operation, a large part of the CaO in the particle has already been carbonated before the particles are heated to the 700 °C while in the CaL thermochemical heat storage system, the entire heat release (carbonation) process is expected to proceed over 700°C. Consequently, the isothermal TGA method is used to study the carbonation kinesics features. The particles are calcinated in the pure argon firstly and then be carbonated in pure CO_2 inside the TGA device under 700 °C, 725 °C, 750 °C, 775 °C, and 800 °C, respectively. Using Eq. (7) and the TGA data, the real-time carbonation conversion under different temperatures can be calculated.

By integrating both sides of the formula, Eq. (5) can be rewritten as:

$$G(\alpha)=\int_0^{\alpha}\frac{1}{f(\alpha)}d\alpha=\int_0^{t}A\frac{A_sM}{D^2}\exp\left(-\frac{E}{RT}\right)\left(\frac{P_{CO_2}-P_{equ}}{P_{atm}}\right)^{m_0}dt=kt \tag{8}$$

As Eq. (8) shows, the G(α)-t curve will be a straight line in the diagram if the isothermal TGA data is plugged into the right mechanism function. Various typical mechanism functions [41-43] are introduced to trial but none of them attain a straight line in G(α)-t diagram. Therefore, intensive efforts are made to build an empirical mechanism function to phenomenologically describe the carbonation reaction. Two more parameters (a and b) are added into $SB(m, n)$ model [44, 45] to increase the freedom degree so that the modified mechanism model is capable to fit better with the tested dα/dt-α curve, the used model function is given in Eq. (9)

$$f(\alpha)=a\cdot\alpha^{m}\left(b-\alpha\right)^{n} \tag{9}$$

The parameter a directly determine the magnitude of f(α) and b is one of the zeros of this function. In typical $SB(m, n)$ model, both their values are 1. Herein, the carbonation process exhibits different kinetic features in different reaction stages thus

this model is used in multiple segmented reaction phases and larger value ranges are needed for parameters *a* and *b*. The segmentation ranges of the mechanism functions are determined by the curve profiles. As the dα/dt-α diagrams show, there are two inflection points during the carbonation process. The first inflection point appears around α of 0.75, where the reaction rate switches from accelerated decline to decelerated decline. Another inflection point locates around α of 0.83 since the decline trend of dα/dt-α diagram changes again at this point. According to these two inflection points, the carbonation process is segmented into three stages: α=0-0.75; 0.75-0.83; 0.83-0.93. Three model functions ($f_1(\alpha)$, $f_2(\alpha)$, $f_3(\alpha)$) are calculated, and their formulas are given in Eq. (10). Both of the fitting results of these model functions and the experimental data are illustrated in Fig. 9. Since there is no intersection between curves $f_1(\alpha)$ and $f_2(\alpha)$, a linear function ($f_{1\text{-}2}(\alpha)$) tangent to both these curves is used to connect these two curves.

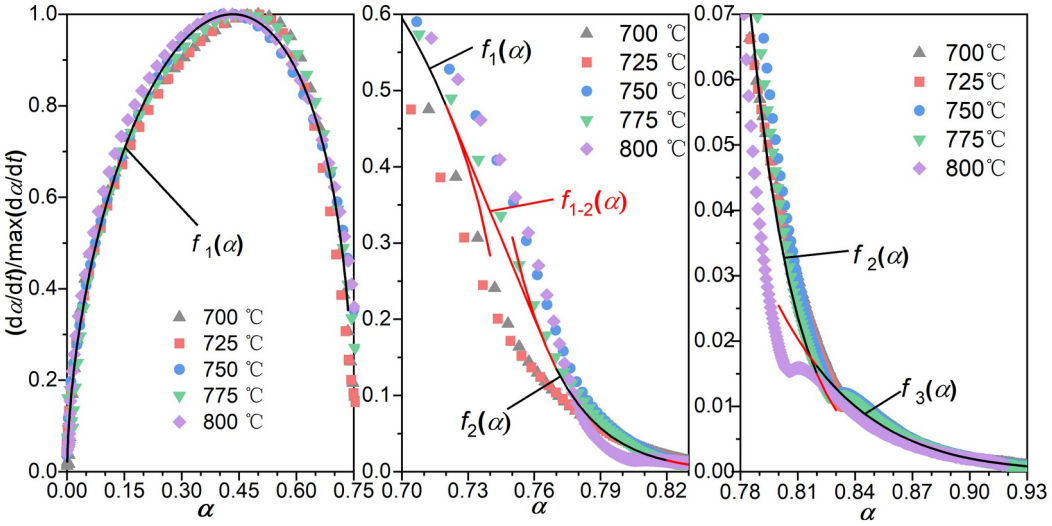

Fig. 9 The dα/dt-α diagrams and fitting curves in different segmented ranges

$$f(\alpha)=\begin{cases} f_1(\alpha)=2.666\alpha^{0.585}\left(0.748-\alpha\right)^{0.424}, & 0\le\alpha<0.720 \\ f_{1-2}(\alpha)=-6.975\alpha+5.503, & 0.720\le\alpha<0.765 \\ f_2(\alpha)=19854.559\alpha^{3.959}\left(1.256-\alpha\right)^{17.905}, & 0.765\le\alpha<0.817 \\ f_3(\alpha)=396.421\alpha\left(1.332-\alpha\right)^{14.058}, & 0.817\le\alpha<1 \end{cases} \tag{10}$$

According to the segmented mechanism function, the isothermal carbonation

reaction of the prepared particle can be roughly divided into three stages: rapid reaction stage, transition stage, and slow reaction stage. In the initial state, there are a great amount of hole structures throughout the composite CaO particle, which benefits the transport of CO_2 from outside to the interior of the particle. However, these gas transfer channels gradually clog and close during carbonation process because the produced $CaCO_3$ has larger cell size than CaO and the volume of solid phase keeps expanding as the conversion rate increasing. After the transition stage, the holes on the particle surface are almost entirely closed and the mass transfer proceeds mainly through the ion diffusion.

The G(α)-t curves of carbonation processes at 700 °C, 725 °C, 750 °C, 775 °C, and 800 °C are presented in Fig. 10. The G(α) data are handled through linear fitness and the results are exhibited in the legend of the figure. The slopes of these lines are the values of k (in Eq. (8)) under relevant temperatures.

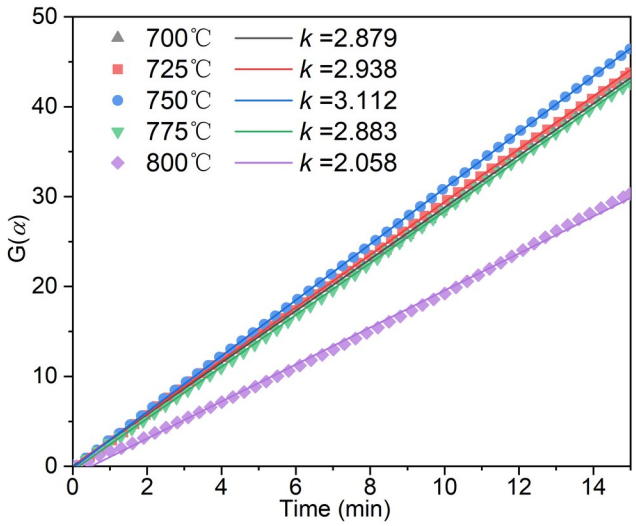

Fig. 10 The G(α)-t diagrams at different temperatures and relevant fitting results

Eq. (8) can also be written as:

$$\ln(k) - m_0 \ln\left(\frac{P_{CO_2} - P_{equ}}{P_{atm}}\right) = \ln\left(A\frac{A_s M}{D^2}\right) - \frac{E}{R}\cdot\frac{1}{T} \tag{11}$$

The fitting results of $\ln(k)$-$m\ln((P_{CO2}-P_{equ})/P_{atm})$ to $1/T$ with different values of m_0 are also presented in Fig. 11. When m_0=5, the coefficient of determination (R^2) reaches up to 0.99. According to Eq. (11) and the $\ln(k)$-$m_0\ln((P_{CO2}-P_{equ})/P_{atm})$-$1/T$

diagram (Fig. 11), the activation energy can be computed using the slope of the curve, and the pre-exponential factor can be calculated using the intercept of the curve on the vertical axis. The computation results show that the apparent activation energy is 65.4 kJ/mol and the pre-exponential factor is 3.48 min^{-1}. With the kinetic triplets, the carbonation kinetic equation is obtained and expression is given in Eq. (12):

$$\frac{d\alpha}{dt} = 3.48\frac{A_s M}{D^2}\exp\left(-\frac{65368.54}{RT}\right)\left(\frac{P_{CO_2}}{P_{atm}} - 4.137\times10^{7}\exp\left(-\frac{20474}{T}\right)\right)^{5} f(\alpha) \quad (12)$$

where the mechanism function $f(\alpha)$ is given in Eq. (10). The complex physical and chemical processes inside the composite porous particle are reflected by an empirical mechanism model $f(\alpha)$, thus the computed kinetic triplets (A, E, $f(\alpha)$) have no specific physical meaning. The exothermic reaction rate of the prepared Ca-based porous particle inside the carbonator can be calculated with this kinetic equation. Meanwhile, the influences of the particle morphology (A_s, M, and D) and operating conditions (P_{CO2} and T) on the carbonation (heat release) process are clarified by this reaction kinetic equation.

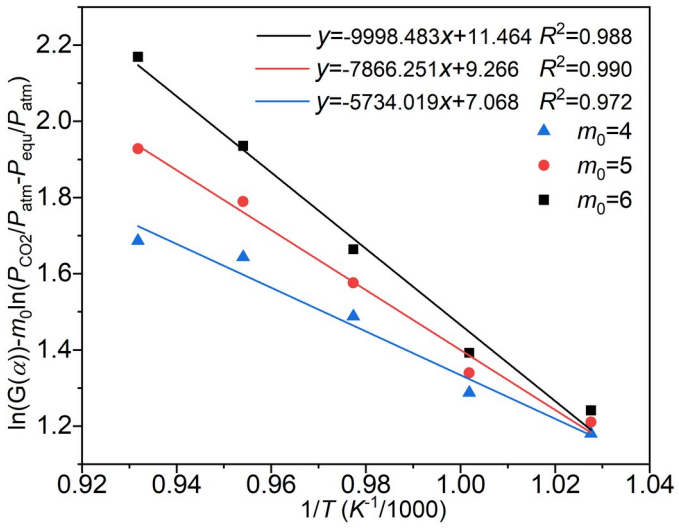

Fig. 11 The ln(k)-$m_0$ln((P_{CO2}-P_{equ})/P_{atm}) versus 1/T diagram

5 Conclusions

By doping Mn-Fe oxides into Ca-Al particles, a new kind of Ca-based composite particle is prepared and it shows benign solar absorbing capability (solar absorptance over 79%). Besides, ASF (for the first time) and MCC are used as templates to

generate pores inside the particles. With the pore-making process, the cyclic stability and carbonation rate of the composite particles are markedly promoted. There is a trade-off between cyclic performance and mechanical strength: a larger amount of the added template attributes to higher cyclic stability and conversion rate, but excessive-high porosity also declines the anti-crushing strength of particles. A reasonable template doping amount and doping ratio are founded in this work. The heat release efficiency of the proposed sample (100-15-6-12-1.5-0.5) stays over 90% in 15 cycles and the conversion rate reaches 80% in 38s, meanwhile, the mean anti-crushing strength (1.95 N) is high enough to withstand continuous collisions and frictions in the operation. The isothermal carbonation kinetic features of the particles are studied and the influencing factors like CO_2 partial pressure, reaction temperature, and particle morphology are considered. Through the regression analyses on the experimental data, a kinetic model is established for the application in the design and regulation of the carbonator in the CaL thermochemical heat storage system.

Acknowledgments

This work was supported by the National Natural Science Foundation of China (No. 51820105010). YM and TL also want to thank the support from Basic Science Center Program for Ordered Energy Conversion of the National Natural Science Foundation of China (No. 51888103) and Natural Science Foundation of Jiangsu Province (No. BK20202008).

References

[1] Liu M, Steven Tay N H, Bell S, et al. Review on concentrating solar power plants and new developments in high temperature thermal energy storage technologies. Renewable and Sustainable Energy Reviews, 2016, 53: 1411-32.

[2] Sarvghad M, Delkasar Maher S, Collard D, et al. Materials compatibility for the next generation of Concentrated Solar Power plants. Energy Storage Materials, 2018, 14: 179-98.

[3] Sukhatme S P, Nayak J. Solar energy. McGraw-Hill Education, 2017.

[4] Stekli J, Irwin L, Pitchumani R. Technical challenges and opportunities for concentrating solar power with thermal energy storage. Journal of Thermal Science and Engineering Applications, 2013, 5: 021011.

[5] Liang J, Li F, Cheng H-M. On Energy: Clean conversion and smart storage in the future. Energy Storage Materials, 2016, 3: A1-A2.

[6] De Meyer O, Dinter F, Govender S. Thermal resistance model for CSP central receivers; proceedings of the AIP Conf Proc, F, 2016. AIP Publishing.

[7] Prieto C, Cooper P, Fernández A I, et al. Review of technology: Thermochemical energy storage for concentrated solar power plants. Renewable and Sustainable Energy Reviews, 2016, 60: 909-29.

[8] Sarrión B, Perejón A, Sánchez-Jiménez P E, et al. Role of calcium looping conditions on the performance of natural and synthetic Ca-based materials for energy storage. Journal of CO2 Utilization, 2018, 28: 374-84.

[9] Chacartegui R, Alovisio A, Ortiz C, et al. Thermochemical energy storage of concentrated solar power by integration of the calcium looping process and a CO2 power cycle. Applied Energy, 2016, 173: 589-605.

[10] André L, Abanades S, Flamant G. Screening of thermochemical systems based on solid-gas reversible reactions for high temperature solar thermal energy storage. Renewable and Sustainable Energy Reviews, 2016, 64: 703-15.

[11] Bayon A, Bader R, Jafarian M, et al. Techno-economic assessment of solid-gas thermochemical energy storage systems for solar thermal power applications. Energy, 2018, 149: 473-84.

[12] Ortiz C, Chacartegui R, Valverde J M, et al. Power cycles integration in

concentrated solar power plants with energy storage based on calcium looping. Energy Convers Manage, 2017, 149: 815-29.
[13] Sarrion B, Valverde J M, Perejon A, et al. On the Multicycle Activity of Natural Limestone/Dolomite for Thermochemical Energy Storage of Concentrated Solar Power. Energy Technology, 2016, 4: 1013-9.
[14] Reich L, Yue L, Bader R, et al. Towards Solar Thermochemical Carbon Dioxide Capture via Calcium Oxide Looping: A Review. Aerosol and Air Quality Research, 2014, 14: 500-14.
[15] Zhai R, Li C, Qi J, et al. Thermodynamic analysis of CO2 capture by calcium looping process driven by coal and concentrated solar power. Energy Convers Manage, 2016, 117: 251-63.
[16] Edwards S E B, Materić V. Calcium looping in solar power generation plants. Sol Energy, 2012, 86: 2494-503.
[17] Teng L, Xuan Y, Da Y, et al. Modified Ca-Looping materials for directly capturing solar energy and high-temperature storage. Energy Storage Materials, 2020, 25: 836-45.
[18] Rodríguez N, Alonso M, Abanades J C. Experimental investigation of a circulating fluidized-bed reactor to capture CO2 with CaO. AIChE Journal, 2011, 57: 1356-66.
[19] Barker R. The reversibility of the reaction CaCO3⇄ CaO+ CO2. Journal of applied Chemistry and biotechnology, 1973, 23: 733-42.
[20] Nikulshina V, Gebald C, Steinfeld A. CO2 capture from atmospheric air via consecutive CaO-carbonation and CaCO3-calcination cycles in a fluidized-bed solar reactor. Chemical Engineering Journal, 2009, 146: 244-8.
[21] Lorsch H G, Kauffman K W, Denton J C. Thermal energy storage for solar heating and off-peak air conditioning. Energy conversion, 1975, 15: 1-8.
[22] Peng W, Xu Z, Luo C, et al. Tailor-Made Core-Shell CaO/TiO2-Al2O3 Architecture as a High-Capacity and Long-Life CO2 Sorbent. Environ Sci Technol, 2015, 49: 8237-45.
[23] Chen J, Shi T, Duan L, et al. Microemulsion-derived, nanostructured CaO/CuO composites with controllable particle grain size to enhance cyclic CO2 capture performance for combined Ca/Cu looping process. Chemical Engineering Journal, 2020, 393: 124716.
[24] Nunes C, Teixeira V, Prates M, et al. Graded selective coatings based on chromium and titanium oxynitride. Thin Solid Films, 2003, 442: 173-8.
[25] Yin Y, Pan Y, Hang L, et al. Direct current reactive sputtering Cr–Cr2O3 cermet solar selective surfaces for solar hot water applications. 2009, 517: 1601-6.
[26] Barshilia H C, Kumar P, Rajam K, et al. Structure and optical properties of Ag–Al2O3 nanocermet solar selective coatings prepared using unbalanced magnetron sputtering. Solar Energy Materials and Solar Cells, 2011, 95: 1707-15.
[27] Esposito S, Antonaia A, Addonizio M L, et al. Fabrication and optimisation of highly efficient cermet-based spectrally selective coatings for high operating

temperature. Thin Solid Films, 2009, 517: 6000-6.
[28] Xue Y, Wang C, Wang W, et al. Spectral properties and thermal stability of solar selective absorbing AlNi–Al2O3 cermet coating. Sol Energy, 2013, 96: 113-8.
[29] Cuevas A, Martínez L, Romero R, et al. Electrochemically grown cobalt-alumina composite layer for solar thermal selective absorbers. Solar Energy Materials and Solar Cells, 2014, 130: 380-6.
[30] Antzara A N, Arregi A, Heracleous E, et al. In-depth evaluation of a ZrO2 promoted CaO-based CO2 sorbent in fluidized bed reactor tests. Chemical Engineering Journal, 2018, 333: 697-711.
[31] Sun P, Grace J, Lim C, et al. The effect of CaO sintering on cyclic CO2 capture in energy systems. AIChE Journal, 2007, 53: 2432-42.
[32] Liu W, An H, Qin C, et al. Performance Enhancement of Calcium Oxide Sorbents for Cyclic CO2 Capture—A Review. Energy & Fuels, 2012, 26: 2751-67.
[33] Sreenivasulu B, Sreedhar I, Reddy B M, et al. Stability and Carbon Capture Enhancement by Coal-Fly-Ash-Doped Sorbents at a High Temperature. Energy & Fuels, 2017, 31: 785-94.
[34] Fedunik-Hofman L, Bayon A, Donne S W. Comparative Kinetic Analysis of CaCO3/CaO Reaction System for Energy Storage and Carbon Capture. Applied Sciences, 2019, 9: 4601.
[35] Arias B, Cordero J M, Alonso M, et al. Sulfation rates of cycled CaO particles in the carbonator of a Ca-looping cycle for postcombustion CO2 capture. AIChE Journal, 2012, 58: 2262-9.
[36] Xu Q, Liu X, Xuan Y, et al. High-performance infrared thermal radiation suppression metamaterials enabling inhibited infrared emittance and decreased temperature simultaneously. Int J Heat Mass Transf, 2020, 161:
[37] Fedunik-Hofman L A, Bayon A, Lipinski W, et al. Investigation of novel hydroxyapatite-doped CaO material for calcination-carbonation thermochemical energy storage; proceedings of the AIP Conf Proc, F, 2018. AIP Publishing LLC.
[38] Shulman A, Cleverstam E, Mattisson T, et al. Manganese/Iron, Manganese/Nickel, and Manganese/Silicon Oxides Used in Chemical-Looping With Oxygen Uncoupling (CLOU) for Combustion of Methane. Energy & Fuels, 2009, 23: 5269-75.
[39] Peng W, Xu Z, Zhao H. Batch fluidized bed test of SATS-derived CaO/TiO2–Al2O3 sorbent for calcium looping. Fuel, 2016, 170: 226-34.
[40] Al-Shankiti I A, Bayon A, Weimer A W. Reduction kinetics of hercynite redox materials for solar thermochemical water splitting. Chemical Engineering Journal, 2020, 389: 124429.
[41] Brown M E, Dollimore D, Galwey A K. Reactions in the solid state. Elsevier, 1980.
[42] Šesták J. Thermophysical properties of solids: their measurements and theoretical thermal analysis. Elsevier, 1984.
[43] Galwey A K, Brown M E. Thermal decomposition of ionic solids: chemical

properties and reactivities of ionic crystalline phases. Elsevier, 1999.
[44] Šesták J, Málek J. Diagnostic limits of phenomenological models of heterogeneous reactions and thermal analysis kinetics. Solid State Ionics, 1993, 63-65: 245-54.
[45] Koga N, Malek J, Sestak J, et al. Data Treatment in Non-isothermal Kinetics and Diagnostic Limits of Phenomenological Models. Netsu Sokutei, 1993, 20: 210-23.